Title

Global Microphysical Sensitivity of Superparameterized Precipitation Extremes

Journal

Earth and Space Science, 8(5)

ISSN

2333-5084

Authors

Charn, Alexander B
Collins, William D
Parishani, Hossein
et al.

Publication Date

2021-05-01

DOI

10.1029/2020ea001308

Peer reviewed

Earth and Space Science

RESEARCH ARTICLE
10.1029/2020EA001308

Global Microphysical Sensitivity of Superparameterized Precipitation Extremes

Alexander B. Charn[1,2], William D. Collins[1,2], Hossein Parishani[3,4], and Mark D. Risser[2]

[1]Department of Earth and Planetary Science, University of California, Berkeley, CA, USA, [2]Division of Climate and Ecosystem Sciences, Lawrence Berkeley National Laboratory, Berkeley, CA, USA, [3]Department of Earth System Science, University of California, Irvine, CA, USA, [4]Now at Ansys Inc., University of California, Irvine, CA, USA

Key Points:

- The choice of microphysics, mainly the number of moments, impacts the statistics of precipitation extremes in a superparameterized model
- Local differences manifest on short time scales (5 days), particularly in the tropics, due to disparities in column-integrated mass fluxes
- Large-scale circulation feedbacks are comparable to local effects in the tropics and are dominant at higher latitudes

Supporting Information:

Supporting Information may be found in the online version of this article.

Correspondence to:

A. B. Charn,
alexcharn5@berkeley.edu

Citation:

Charn, A. B., Collins, W. D., Parishani, H., & Risser, M. D. (2021). Global microphysical sensitivity of superparameterized precipitation extremes. *Earth and Space Science*, *8*, e2020EA001308. https://doi.org/10.1029/2020EA001308

Received 18 JUN 2020
Accepted 24 MAR 2021

Abstract A recent study found statistically significant differences in extreme precipitation distributions over the contiguous United States (CONUS) when changing the microphysics scheme in a superparameterized global climate model. Here, we repeat the analysis globally and similarly find that differences are widespread when varying the number of predicted moments in the microphysics parameterization, but not when comparing variants of the double-moment scheme. However, contrary to the previous study in which differences largely disappeared over CONUS when 5-day simulations were conducted, we found that the signal in these shorter integrations remains within the tropics, implying a direct local effect of microphysics on precipitation extremes in these regions. The effect on precipitation is traced back to changes in vertical velocity profiles changes that are then amplified in the climatological simulations compared to the 5-day ones. Finally, the superparameterized extremes, regardless of the microphysics scheme, are shown to be larger than those from the Global Precipitation Climatology Project One-Degree Daily data set and generally smaller than those from the Tropical Rainfall Measuring Mission 3B42 data set.

1. Introduction

Precipitation extremes are expected to increase with climate change (Held & Soden, 2006; Romps, 2011). Retrospective analyses of storms such as Hurricanes Harvey (Risser & Wehner, 2017), Katrina, Irma, and Maria (Patricola & Wehner, 2018) concluded that increased atmospheric temperatures likely led to more rainfall than would have been expected in a counterfactual world with no anthropogenic climate change. Despite their general skill at reproducing mean precipitation patterns on large spatial scales, global climate models (GCMs) still have difficulty representing extremes and even first-order phenomena such as the Intertropical Convergence Zone (ITCZ) (Flato et al., 2013). One reason is that the atmospheric convection that generates clouds and precipitation must be parameterized, as opposed to explicitly simulated, since the characteristic length scales of these processes are much smaller than a conventional GCM grid cell. Typical GCMs often diagnose convection and its effects by assuming a quasi-steady equilibrium (e.g., Zhang & McFarlane, 1995), an approximation that is notorious for underestimating higher-intensity updrafts and hence, extreme rainfall (Dai, 2006; Wilcox & Donner, 2007). Convective parameterizations have also been heavily implicated in the so-called "double ITCZ" problem, where a spurious band of precipitation south of the Equator, comparable to its northern counterpart, appears in the annual mean (Hirota et al., 2011; Woelfle et al., 2018).

One alternative to the use of convective parameterizations that balances resolution and computational cost is the utilization of a superparameterized (SP) model such as the SP version of the Community Atmosphere Model (CAM), known as SPCAM (Khairoutdinov & Randall, 2001). Superparameterization replaces the moist physics parameterizations in each GCM grid column with a cloud-resolving model (CRM). Depending on its resolution, the CRM can resolve deep-convective and mesoscale processes in response to large-scale GCM dynamics, in return providing subgrid convective heating and moistening tendencies to the larger grid. Thus, cloud-scale interactions between cloud dynamics, microphysics, radiation, and turbulence are more finely resolved. Various studies have documented improved correlation with observations, for example, of the Madden-Julian Oscillation (Benedict & Randall, 2009), African easterly waves (McCrary et al., 2014), and global precipitation distributions (Kooperman et al., 2016). Li et al. (2012) also documented an improved representation of rainfall, but within the contiguous United States (CONUS) and

Table 1
Summary of Microphysics Experiments Performed

Name	SAM scheme	Rimed-ice species	Size threshold in raindrop breakup process (μm)
1MG	1MOM	Graupel	n/a
2MG300	M2005	Graupel	300
2MH300	M2005	Hail	300
2MG600	M2005	Graupel	600

SAM, System for Atmospheric Modeling.

with a focus on extremes, and with the caveat that SP extremes were still unable to fully match the magnitude of those observed via rain gauges in the southern United States.

While the structural uncertainties associated with the representation of convection have been examined by comparing simulations from CAM to those from SPCAM, less attention has been paid to the parametric uncertainty that arises due to the representation of cloud microphysics in global models. See Charn et al. (2020) or Elliott et al. (2016) for a discussion of microphysical sensitivities within limited-domain CRMs. To the best of our knowledge, these two studies are also the only ones to have examined the effects of different parameterizations of microphysics within the SPCAM framework. Elliott et al. (2016) investigated summertime mesoscale convective systems (MCSs) within CONUS and found that sensitivities in MCS event counts and precipitation rates were overshadowed by interannual variability. Charn et al. (2020) looked at extreme precipitation within CONUS and found significant differences, mostly when comparing one-moment and two-moment microphysics schemes, as a result of feedbacks onto the large-scale circulation.

Here, we generalize our analysis from that of Charn et al. (2020) to global precipitation rates. We again ask whether any significant differences are due to local effects or feedbacks on the large-scale circulation. While the latter was found to dominate the signal within CONUS, there is reason to expect the former's importance within the tropics. Fan et al. (2015) found vertical profiles of mass fluxes in their CRM to be insensitive to the choice of microphysics in two short-integration (24 h) midlatitude case studies, but strongly affected in a tropical case. They argued that the strong large-scale dynamic forcing constrained the mass fluxes in the midlatitudes, but the upscale feedback of microphysics onto the convective organization was key in determining the flux profiles in the tropical case.

2. Data and Methods

2.1. SPCAM

We have employed SP-CAM, where CAM is the atmospheric component of the Community Earth System Model (Hurrell et al., 2013), forced by prescribed monthly sea-surface temperatures (SSTs) and sea ice boundary conditions (a run-time configuration known as the F_2000 compset). The embedded CRM is the System for Atmospheric Modeling (SAM) (Khairoutdinov & Randall, 2003). There are two fundamentally different microphysics parameterizations within SAM: The original, one-moment scheme (1MOM in Table 1) described in Khairoutdinov and Randall (2003) and the two-moment one (M2005 in Table 1) from Morrison et al. (2005). The microphysics experiments conducted are summarized in Table 1. Two minor modifications are tested within M2005: 2MH300, where the default rimed-ice species is hail instead of graupel, and 2MG600, where the threshold diameter in the raindrop breakup/self-collection process implemented following Verlinde and Cotton (1993) has been increased from the default of 300 to 600 μm. The reader can refer to Charn et al. (2020) for more details about the model configuration and the microphysics schemes. Precipitation rates have been output every 3 h, and to be clear, average rates (equivalent to accumulation over the 3-h time period), as opposed to instantaneous rates every 3 h, were output. As in Charn et al. (2020), the 2MG300 case is considered the baseline, and comparisons will be made between it and the other three in turn. All figures plotting a difference in return values between two microphysics schemes will have that of 2MG300 as the minuend (quantity being subtracted from) and that of the other case as the subtrahend (quantity being subtracted).

2.2. Experiment Design

2.2.1. Climatological Runs

The 7-year climatological runs used for this analysis are those conducted by Charn et al. (2020). The integrations have start dates on June 1, 1991, and end dates on November 30, 1998, with the first six months

discarded to remove spinup effects. The annually cyclic, present-day climatological (1982–2001) SST and sea ice boundary conditions originally from Hurrell et al. (2008) are used.

2.2.2. InitiaLIzed-Ensemble, Analyze, and Develop

To determine whether the results seen in the climatological runs are due to differing immediate, local effects or the microphysics' feedback on the large-scale circulation, we make use of the InitiaLIzed-ensemble, Analyze, and Develop (ILIAD) framework introduced by O'Brien et al. (2016). This software was created to assess the effects of different model parameterizations or resolutions by conducting repeated, short hindcast simulations initialized with reanalysis output and comparing the results against the meteorological conditions observed during the hindcast period. Here, however, instead of using reanalysis outputs, each simulation is initialized with output from the 1MG and 2MG300 climatological runs. This will allow us to avoid the potentially confounding factor of Climate Forecast System reanalysis output (Saha et al., 2010) containing zero land ice, in contrast to the monthly climatological data used in the free-running experiments. It will also enable us to assess any sensitivity to the source of the initial conditions. The experimental protocol of O'Brien et al. (2016), which we also use here, consists of one 5-day integration initialized at 00Z every day for 5 years. Precipitation output is taken from the fifth simulation day, a timeframe that allows the model to develop a somewhat distinctive dynamical state yet still be constrained to that of the initial condition.

2.3. Observations

To assess the fidelity of SPCAM's precipitation extremes, we make use of two observational data sets. The first is the Global Precipitation Climatology Project (GPCP) One-Degree Daily (1DD) Precipitation Data Set, version 1.2, hereafter GPCP 1DD (Huffman et al., 2001). From 40°S to 40°N, GPCP 1DD precipitation is calculated from the Threshold-Matched Precipitation Index, which ingests infrared brightness temperatures observed by geosynchronous and low-earth-orbit satellites. At higher latitudes, GPCP 1DD values are calculated using a multiple-regression relationship between rain gauge measurements and cloud parameters derived from Television and Infrared Observation Satellite Operational Vertical Sounder instruments. We also compare our results from SPCAM with data from the Tropical Rainfall Measuring Mission (TRMM), specifically its Multi-satellite Precipitation Analysis (TMPA) product 3B42, version 7, hereafter TRMM 3B42 (Huffman et al., 2007). TRMM 3B42 precipitation is derived using three of its own instruments (the TRMM Microwave Imager, the VIS/IR Radiometer, and the Precipitation Radar), combined with microwave measurements from other satellites. It is available as a 0.25°, 3-hourly instantaneous product between 50°S and 50°N. As in Kooperman et al. (2016), we compare SPCAM to the observational products by aggregating model output and TRMM data to daily resolution. We employ 5 years of data from December 1, 1998, to November 30, 2003, for both sets of observations.

2.4. Comparison Procedure

To compare precipitation extremes, extreme value distributions (EVDs) were fitted to 3-h data for each grid cell. Specifically, we employed the non-homogeneous Poisson point (NHPP) process (Pickands III, 1971), also referred to as peaks-over-threshold (POT), referring to the fact that it models all extreme values greater than a specified threshold, subject to temporal de-clustering (described below). Other possible EVDs that could have been used include the Generalized Extreme Value and the Generalized Pareto distributions; see Charn et al. (2020) for a discussion on how the NHPP was selected, as well as a mathematical description. We used the likelihood ratio test to determine whether the fitted NHPP processes are significantly different from each other. This involves first calculating the test statistic:

$$z = -2\ln\frac{\sup\{L(\theta_{12}\,|\,x_1,x_2)\}}{\sup\{L(\theta_1 \mid x_1)\}\sup\{L(\theta_2 \mid x_2)\}}, \tag{1}$$

where the numerator refers to the NHPP process fitted to the extremes from both microphysics cases "1" and "2," and the denominator refers to the processes fitted individually to the two cases. S.S. Wilks (1938) proved that a test statistic of this form asymptotes to a chi-square distribution with k degrees of freedom, where k is the difference in the number of parameters between the null and alternative models. Here, $k = 3$

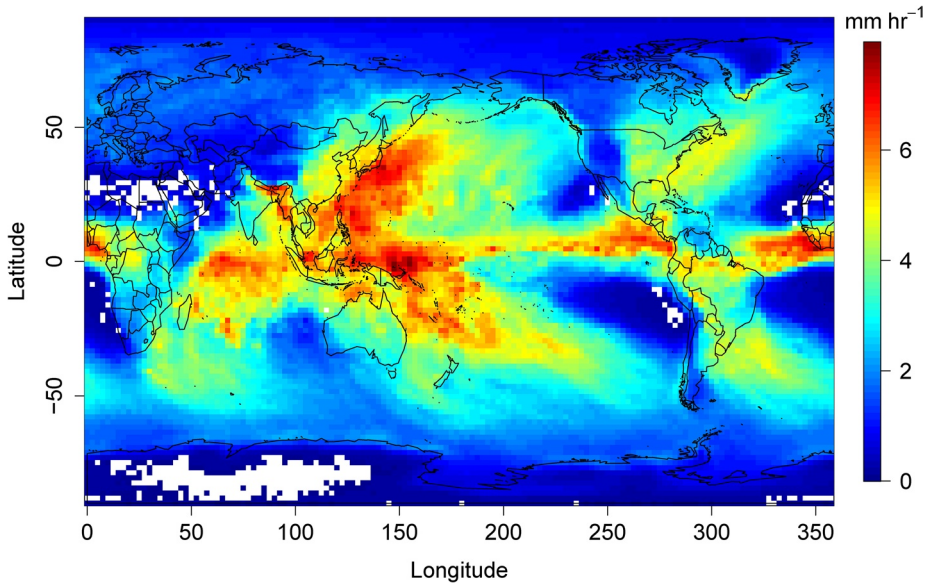

Figure 1. Two-year climatological return value for 2MG300 (Table 1). Grid cells where parameter estimation failed are blank.

since there are three parameters in the null (corresponding to the three parameters in the NHPP process), that is, both distributions can be reasonably described by the same process, and six in the alternative, that is, separate fits for the two distributions.

Because the test statistic requires that the parameter estimation in the numerator and the denominator be done using the same data, the former is found by analyzing the union of the extremes for each individual microphysics case, rather than extremes determined from the union of the whole data sets. This also necessitates a uniform threshold u. Therefore, when comparing two data sets in a given grid cell and a season, in Charn et al. (2020) u was defined as the higher of the two individual 98th percentiles, and extremes for both cases were defined as values greater than u. Here, when doing a global analysis, this led to some dry regions, mostly in northern Africa and the Arabian Peninsula, having a threshold of 0 mm/day. To remedy this, we define u as the higher 90th percentile of rain rates greater than 1 mm/day. Doing this leads to more failures in the optimization algorithm in the aforementioned regions (along with others, e.g., Antarctica), but it does not change the fundamental results (not shown). Finally, to account for temporal clustering, for example, a storm with high rain rates over multiple 3-h periods, we took only the maximum value in each series of consecutive exceedances.

Once the three sets of extremes are acquired, the test statistic and the corresponding p-value can be calculated. As in Charn et al. (2020), we control the false discovery rate (FDR) (Benjamini & Hochberg, 1995) with $\alpha_{\mathrm{FDR}} = 0.05$ in order to account for the effects of multiple-hypothesis testing (conducting individual tests at multiple grid points) (D. S. Wilks, 2016).

3. Results

3.1. Climatological Runs

Figure 1 shows the map of 2-year return values for the climatological 2MG300 simulation. The 2-year return value is the precipitation rate expected to be exceeded once every 2 years, as calculated from the fitted NHPP process within each grid cell; see Charn et al. (2020) for more details. When comparing precipitation extremes (Figure 2), we see that the differences when looking at the number of predicted moments dwarf those when comparing variants of the two-moment scheme. Altering the rimed ice species (Figure 2b) and the raindrop breakup parameter (Figure 2c) results in a handful of significant differences, mostly located between 30°S and 30°N and over the ocean. The limited amount of stippling culminates in a lack of much in

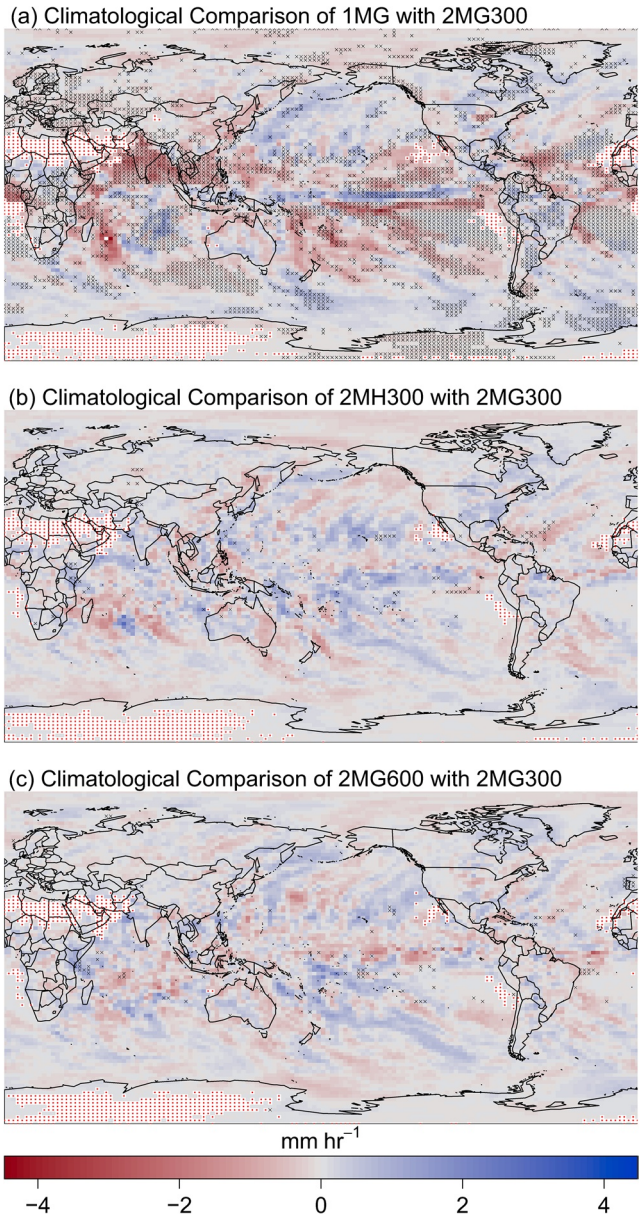

Figure 2. Climatological comparison of (a) 1MG, (b) 2MH300, and (c) 2MG600 with 2MG300 (Table 1). Following the convention defined in Section 2, the quantity plotted is the 2MG300 2-year return value minus that from the other microphysics cases. Grid cells with statistically significant differences between the two extreme precipitation distributions are stippled in black. Grid cells where parameter estimation failed are stippled in red.

terms of a spatially coherent signal. Thus, for the remainder of the paper, we do not delve into the 2MH300 and 2MG600 cases any further.

In contrast, a much larger fraction of grid cells is flagged when comparing 1MG and 2MG300 (Figure 2a). Again, much of the signal is between 30°S and 30°N and over the ocean. However, there is also an appreciable signal over land, including Europe, India, Africa, and South America, as well as at higher latitudes, for example, over the Southern Ocean. Broadly speaking, there is a narrow band of higher precipitation extremes in the 2MG300 experiment around the Equator, flanked by higher extremes in the 1MG run in the subtropical regions, though some exceptions to this trend occur over South America and off the western coasts of Africa and Australia. This is suggestive of a strengthened Hadley circulation when using two-moment microphysics, a topic we will briefly revisit in the next section. There is even evidence of increased uplift over the Southern Ocean, at the southern edge of the Ferrell cell, though such a pattern is less obvious at the corresponding latitude range in the Northern Hemisphere.

Despite the vastly greater number of statistically significant differences when comparing 1MG and 2MG300, the differences in return values are generally comparable in magnitude within the three comparisons in Figure 2. This suggests that return values themselves are not a good indication of whether two extreme precipitation distributions are significantly different. As a comparison to a more traditional definition of extremes, Figure S1a shows the map of annual 99.9th percentile 3-h precipitation rates for 2MG300. There is an extremely tight correlation between this map and that of the 2-year return values, with a correlation coefficient $r = 0.98$. Figure S1b shows the 99.9th percentile of 2MG300 precipitation minus that of 1MG precipitation. Again, the spatial pattern is quite similar to that in Figure 2a, though the correlation with the difference in return values drops off to $r = 0.81$. This is because the threshold that demarcates an extreme, which ultimately influences the calculated return value, in each grid cell is defined as the minimum between that from 1MG and 2MG300, precluding a strict correlation with the straight 99.9th percentile.

3.2. Five-Day Runs

As discussed earlier, 5-day runs were conducted using the ILIAD framework to identify whether the differences in the climatological distributions of extreme precipitation (Figure 2) are due to local effects or feedbacks on the large-scale circulation. Because the differences between the one-moment and two-moment base cases vastly outnumbered those between the two-moment variants, and due to limitations on computational resources, the ILIAD runs were only carried out with 1MG and 2MG300 microphysics. Four sets of simulations were performed: two—one using 1MG and the other using 2MG300—were branched off from the 1MG climatological run. Similarly, two other integrations were branched off from the 2MG300 climatological run. While the simulations using the same microphysics as the source (1MG → 1MG, 2MG300 → 2MG300) are similar to the climatological runs themselves, they are not completely identical because the files used to initialize the 5-day runs contained a subset of the atmospheric fields used in the model's native restart files. Because the results do not depend on the source of the initial conditions, that is, which climatological run the ILIAD simulations were branched from (not shown), the remainder will be devoted to those derived from the 1MG large-scale meteorological conditions.

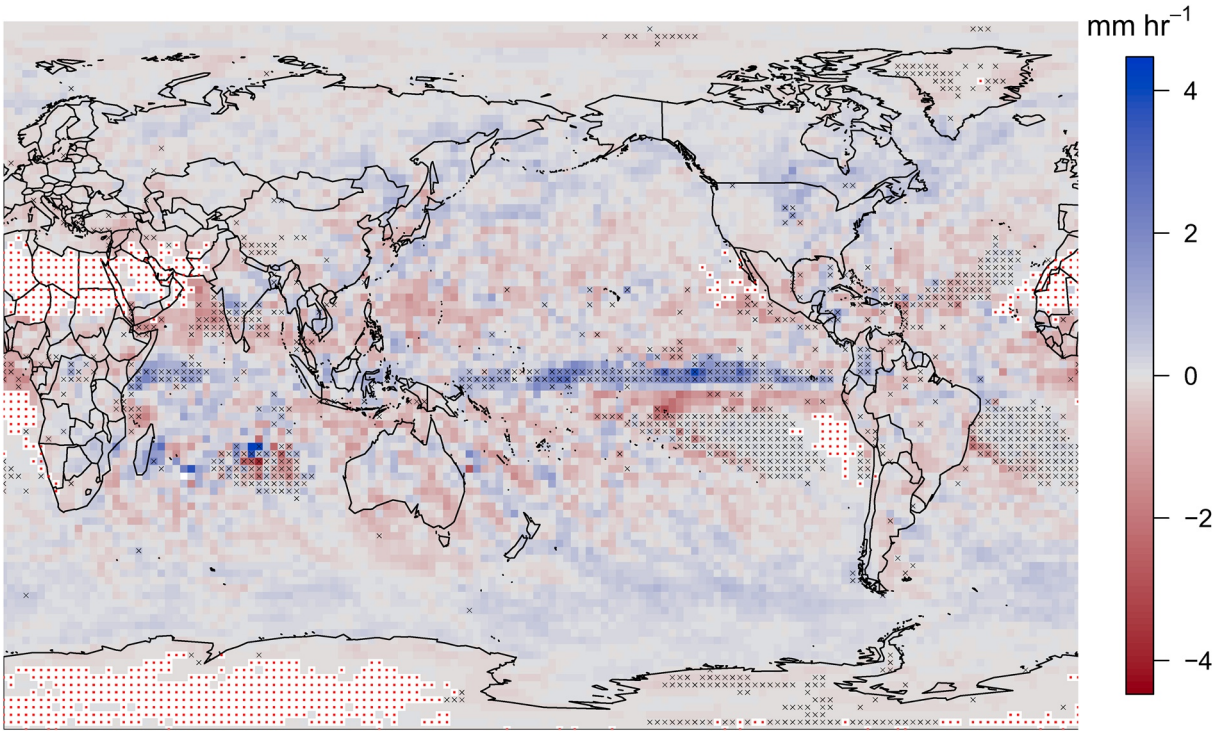

Figure 3. As in Figure 2, but with the comparison of 1MG and 2MG300 (Table 1) extremes within the ILIAD framework. ILIAD, InitiaLIzed-ensemble, Analyze, and Develop.

In the 5-day runs, unlike in Charn et al. (2020), a substantial signal with spatial coherence remains when comparing extreme precipitation between 1MG and 2MG300 (Figure 3). The signal is largely confined to latitudes between 30°S and 30°N. Much of the signal in the Southern Ocean as well as in the northern Pacific has disappeared, as has that in land regions such as Europe, the Indochinese Peninsula, northern India, Canada, and South America. Table 2 quantifies this: The fraction of extratropical cells identified as significantly different drops to almost zero in the 5-day runs. However, we note that in the tropics, the microphysical feedbacks on the large-scale circulation are comparable to the local effects, in the sense that the number of grid cells showing statistically significant differences more than doubles in the climatological simulations (43% vs 18% between 30°S and 30°N).

As mentioned in Section 3.1, the opposing signals in the ascending and descending regimes of the Hadley cell imply a strengthening of the circulation when using the two-moment microphysics scheme, which could impact precipitation. Tao and Chern (2017) discussed a similar phenomenon within their SP model (the Goddard Multiscale Modeling Framework) while investigating sensitivities to CRM domain size. Specifically, a smaller domain with coarser resolution in their embedded CRMs led to a strengthened Hadley cell, which they argued enabled enhanced evaporation in the subtropics, in turn resulting in greater low-level water vapor flux convergence into the tropics. However, given the fact that the Hadley turnover time is on

Table 2
Percentage of Cells With Statistically Significant Differences Between 1MG and 2MG300

	Climatological			ILIAD		
	Land(%)	Ocean(%)	Total(%)	Land(%)	Ocean(%)	Total(%)
30°S–30°N	32	47	43	7	22	18
[a]$\lvert\phi\rvert > 30°$	21	17	18	5	1	2
Total	24	28	26	6	8	7

[a]ϕ denotes latitude.

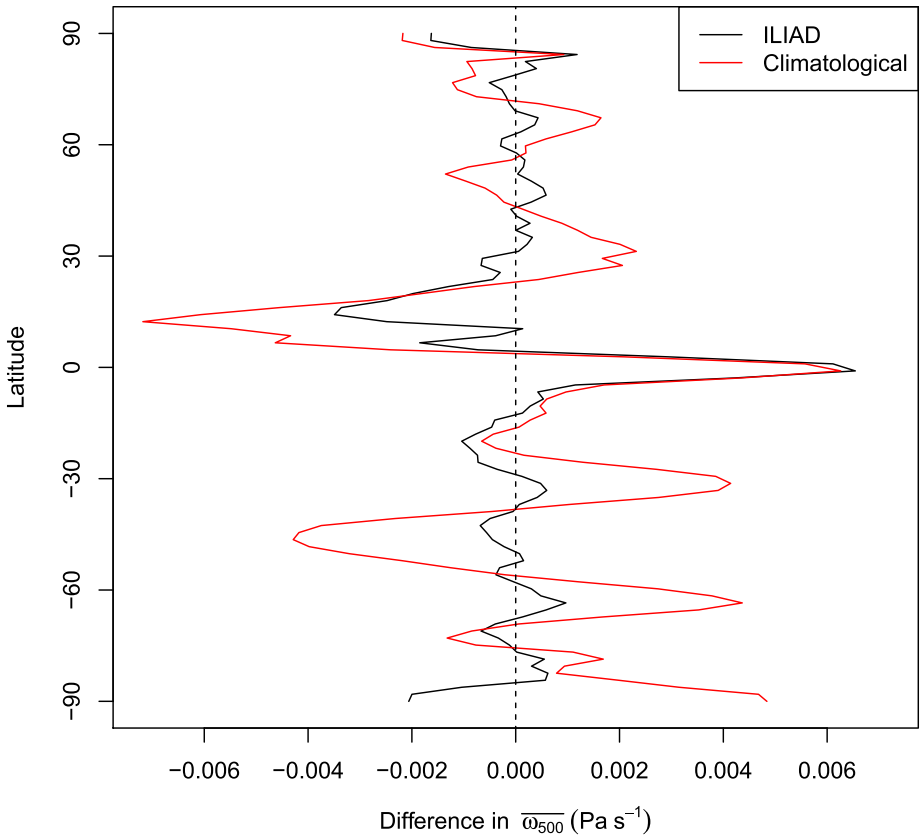

Figure 4. 1MG (Table 1) zonal mean of $\omega_{500\ \mathrm{hPa}}$ minus that of 2MG300.

the order of a month, a time period of 5 days seems insufficient to allow either increased uplift in the deep tropics or increased subsidence in the subtropical regions to impact the other. Unfortunately, output from the first 4 days of each 5-day run was not saved to test this, so we do not explore this further.

3.3. Vertical Velocity

Figure 4 shows the zonal mean of 500-hPa vertical velocity ($\omega_{500\ \mathrm{hPa}}$) from the 1MG case minus that from the 2MG300 case for both the climatological and ILIAD simulations. In the ILIAD runs, the difference in vertical velocity is most appreciable between 30°S and 30°N, with smaller magnitudes at higher latitudes. The 2MG300 microphysics generally leads to enhanced upward motion in the deep tropics around the Equator and enhanced downwelling in the subtropics. In the climatological simulations, where the large-scale circulation has the time to respond in the midlatitudes, differences in vertical velocity are intensified, particularly over the ocean (Figure S2). 1MG microphysics leads to enhanced upward motion around 50°S in the southern parts of the Indian, Pacific, and Atlantic. Around 60°S, the reverse signal is amplified, with 2MG300 displaying greater upward motion throughout the Southern Ocean. The zonal-mean difference in $\omega_{500\ \mathrm{hPa}}$ is weaker in the northern midlatitudes and displays more sign reversals within both the climatological and the ILIAD cases. There is even a sign reversal between climatological and ILIAD at 50°N: Slightly higher upward motion with 2MG300 in the latter is overtaken by higher updrafts in 1MG in Russia, Mongolia, and Europe. Figure 4 lends support to the above results—and those in Charn et al. (2020)—in that changes in vertical velocity and precipitation extremes are appreciable in the tropics in short, 5-day runs, but only significantly appear in the midlatitudes in longer simulations.

To partition thermodynamic and dynamic contributions to extreme precipitation, scaling formulas involving vertical pressure velocity ω and specific humidity q_v (or its saturated value q_v^*) have been previously developed. Both single-level (e.g., O'Brien et al., 2016), which involve products of predictor variables at

specific heights or pressure levels, and full-tropospheric scalings (e.g., O'gorman & Schneider, 2009), which involve integrals of water vapor flux, have been investigated in the literature. Here, we use a full-tropospheric approach, given in Equation 2, to investigate individual extreme precipitation events from the ILIAD integrations, complementing the results in Figure 4.

$$P = S(\omega, q_v^*) = \alpha \int_{1000\text{hPa}}^{200\text{hPa}} \omega \frac{\partial q_v^*}{\partial p} \frac{dp}{g}, \tag{2}$$

where P is the precipitation, α is a precipitation efficiency, chosen so that $P = S(\omega, q_v^*)$ for each microphysics case, and g is gravitational acceleration.

Equation 2 can be rewritten, as in Fildier et al. (2017), as

$$P = S(\omega, q_v^*) = \alpha \underbrace{\langle \omega \rangle}_{M} \left\langle \underbrace{\frac{\omega}{\langle \omega \rangle}}_{\mu} \underbrace{\left(\frac{\partial q_v^*}{\partial p} \right)}_{\gamma} \right\rangle, \tag{3}$$

where the angle brackets denote a vertical integral over the troposphere: $\langle X \rangle = \int_{1000\text{hPa}}^{200\text{hPa}} X \frac{dp}{g}$. Thus, M is the column-integrated mass flux, μ is the normalized mass flux profile, and γ is the vertical gradient in q_v^*. Again as in Fildier et al. (2017), a fractional change in (extreme) precipitation can be written as follows:

$$\delta P = \underbrace{\delta\alpha}_{E} + \underbrace{\delta \mathrm{M}}_{D1} + \underbrace{\frac{\langle \gamma \Delta \mu \rangle}{\langle \gamma \mu \rangle}}_{D2} + \underbrace{\frac{\langle \mu \Delta \gamma \rangle}{\langle \gamma \mu \rangle}}_{T} + N, \tag{4}$$

where ΔX represents a simple difference, $\delta X \equiv \Delta X / |X|$ a fractional difference, and N higher-order terms. Thus, $D1$ is a change in the column-integrated mass flux, $D2$ a change in the shape of the mass-flux vertical profile, and T any thermodynamic contribution to a difference in precipitation.

Here, we calculate E, $D1$, $D2$, and T for each precipitation extreme from the ILIAD simulations. More precisely, for each grid cell flagged as having significantly different extreme precipitation distributions, for each time in which both the 1MG and the 2MG300 rain rates are classified as extreme by our algorithm, the above four quantities are calculated. Simple and fractional differences are calculated with respect to the quantity from the microphysics case with the larger extreme; for example, if a 1MG precipitation rate is identified as the larger extreme, $D1 \equiv \delta M = (M_2 - M_1)/|M_1|$. We choose to only look at times at which both values are extreme in order to minimize the contribution of E, which can be relatively large when comparing an extreme with a non-extreme rain rate, reflecting the loss of accuracy of the scaling in the latter case. Relaxing this criterion and analyzing times at which precipitation is only extreme with one microphysics case is done in Figures S3 and S4 (described below).

Given that most of the statistically significant differences are between 30°S and 30°N, we focus our analysis within this latitude range. Figure 5a shows the zonal median of E, $D1$, $D2$, and T for times when the 1MG extreme is larger, Figure 5b for times when the 2MG300 extreme is larger. Thus, each subplot allows us to infer which term is causing the rain rate from the other case (i.e., 2MG300 in Figure 5a and 1MG in Figure 5b) to be smaller. Because we are not simulating climate change, but rather conducting an experiment with two microphysics schemes in the present day, we would not expect T to have a significant contribution. Indeed, this is confirmed in Figure 5, where T is generally less than 5% in magnitude. $D2$ is also generally associated with climate change: An upward shift of the mass flux profile is expected to accompany the upward shift in the radiative cooling profile (Singh & O'Gorman, 2012; Jeevanjee & Romps, 2018). Still, disparate microphysics schemes might be expected to cause changes not only to the column-integrated mass flux, $D1$, but also to the shape of the vertical profile, $D2$, via differences, for example, in riming and depositional growth, which in turn go on to affect latent heating (Van Weverberg et al., 2012). Nevertheless, the zonal profile of $D2$ is also small in Figure 5, with median values less than 5% in magnitude.

As expected, the contribution of E is relatively small, generally less than 10% in magnitude, though values can reach ~15% at the outer edges of the tropics in Figure 5b. Figure S3 shows the same plots as Figure 5,

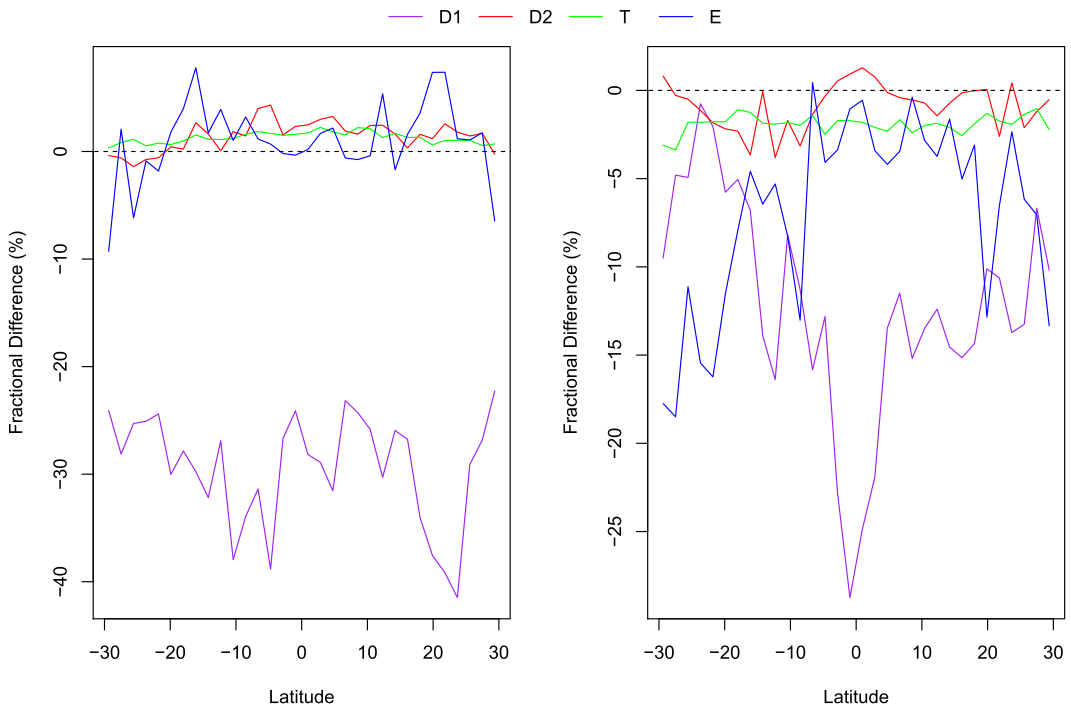

Figure 5. Zonal median of fractional changes of terms in Equation 2 for (left) times when the ILIAD 1MG (Table 1) precipitation extreme is greater than that from 2MG300 and (right) vice versa. Values are only calculated in grid cells with statistically significant differences in the (ILIAD) extreme precipitation distribution. Differences are computed such that negative values represent tendencies for lower column-integrated saturation vapor flux ($S(\omega, q_v^*)$ in Equation 2) in the microphysics case with the *smaller* extreme, for example, 2MG300 in (a) and 1MG in (b). ILIAD, InitiaLIzed-ensemble, Analyze, and Develop.

but is calculated for all extremes within grid cells flagged as having significantly different distributions, regardless of whether the rain rate from the other microphysics scheme is extreme. Figure S4 is the same as Figure S3, but for all grid cells in the tropics. As mentioned above, because it is possible that a rain rate is extreme in one microphysics case but not the other, the scaling in Equation 2 is not expected to hold for the non-extreme case in Figures S3 and S4. Thus, it is not surprising that E values are much higher in magnitude in these cases, reaching upwards of 50% in the subtropics in Figure S3.

The largest contribution is that from $D1$; the median fractional decrease in mass flux is 25%–40% when the 1MG extreme is larger than the corresponding one from 2MG300 (Figure 5a). There is more noise in $D1$ in Figure 5b, with small values in the subtropics. But in the deep tropics where 2MG300 extremes are generally larger (Figure 3), column-integrated mass flux differences are the clear primary contributor. Figure 6 combines the information in Figure 5; here, the signs of all quantities used to compute Figure 5b are reversed, and the median across both cases is taken. Thus, positive values in Figure 6 denote latitudes where the contribution tends to yield higher extremes when using two-moment microphysics. The total contribution, shown by the thick, black line, generally reflects the conclusions in Figure 3: 2MG300 results in higher extremes in a narrow band around the Equator, and the opposite is true in the subtropics. It is interesting to note that the median values of $D2$, T, and E all tend to support higher column-integrated saturation vapor fluxes for 2MG300 everywhere (this can also generally be seen in Figure 5). Only $D1$ shows clear evidence of one-moment extremes being higher in the subtropics, confirming that changes in column-integrated mass fluxes are the primary driver of disparities in the tropical extreme precipitation distributions. This result is consistent with that of Fan et al. (2015), whose CRM domain-mean mass-flux vertical profile varied considerably with microphysics when simulating a mesoscale convective complex (MCC) during the Tropical Warm Pool International Cloud Experiment (but not when modeling an MCC or a squall line during two case studies in the midlatitudes). We note, however, that Fan et al. (2015) argued that microphysical feedbacks to the convection's organization were responsible, whereas we do not investigate the frequency of

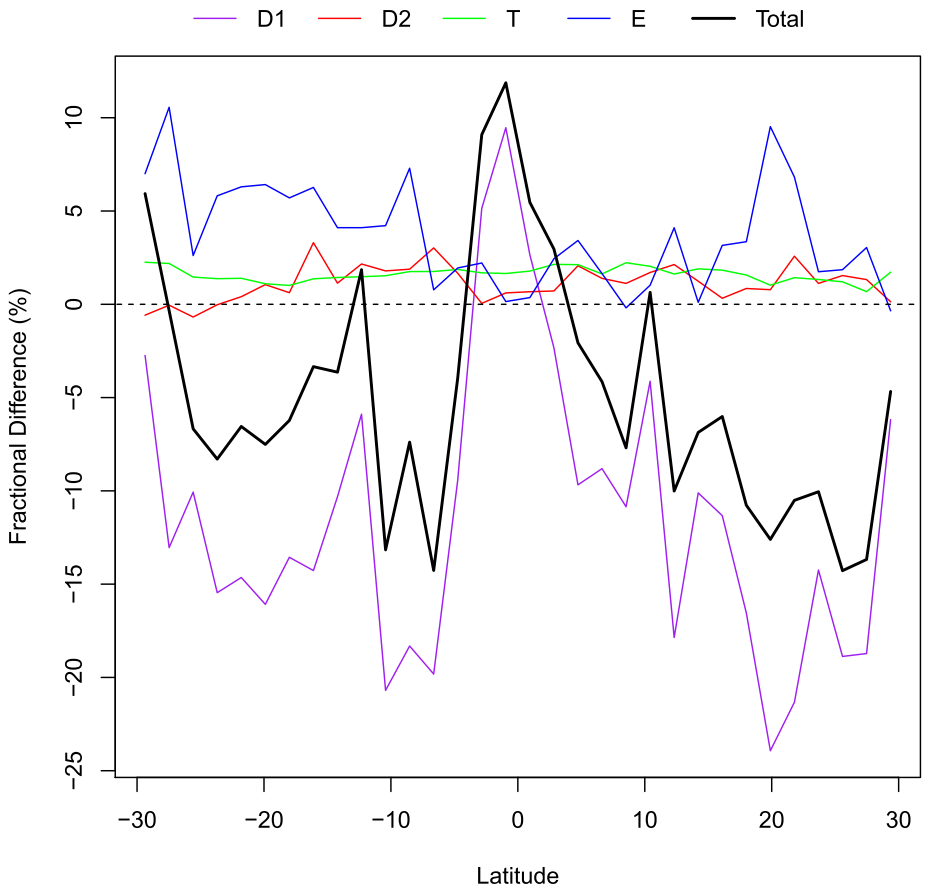

Figure 6. Zonal median of fractional changes of terms in Equation 2 for times when both the 1MG and the 2MG300 (Table 1) precipitation rates are classified as extreme. Positive values represent tendencies for higher column-integrated saturation vapor flux ($S(\omega, q_v^*)$ in Equation 2) for 2MG300. Values are only calculated in grid cells with statistically significant differences in the (ILIAD) extreme precipitation distribution. ILIAD, InitiaLIzed-ensemble, Analyze, and Develop.

such convective organization, though the work of Tao and Chern (2017) suggests convection might generally be more scattered in a CRM domain as small as ours (64 km).

3.4. Estimating Natural Variability of SPCAM Return Values

It is natural to wonder about the impact of interannual variability on our results, particularly in regions such as the subtropics with low annual rainfall, given our relatively short integration period of 5 years for the ILIAD simulations. To test this, we take the same approach as in Charn et al. (2020) by grouping the output into 10 years (consisting of the two microphysics experiments of 5 years each). The 10 years were then randomly reshuffled and the analysis redone. This process was performed 400 times, and the median number of grid cells by latitude marked as statistically significant is plotted in Figure 7. While there is indeed evidence of increased noise in the subtropics, interannual variability is still overwhelmed by the actual signal between 30°S and 30°N.

3.5. Comparing With Observations

Figure 8a (S5) compares the climatological 1MG (2MG300) output with GPCP 1DD and TRMM 3B42. As mentioned in Section 2.3, the observational comparisons were carried out at daily resolution. GPCP 1DD shows lower extremes compared to SPCAM essentially everywhere, notably the Indian Ocean, the western Pacific, the ITCZ, the South Pacific Convergence Zone, and western central Africa. On the other hand,

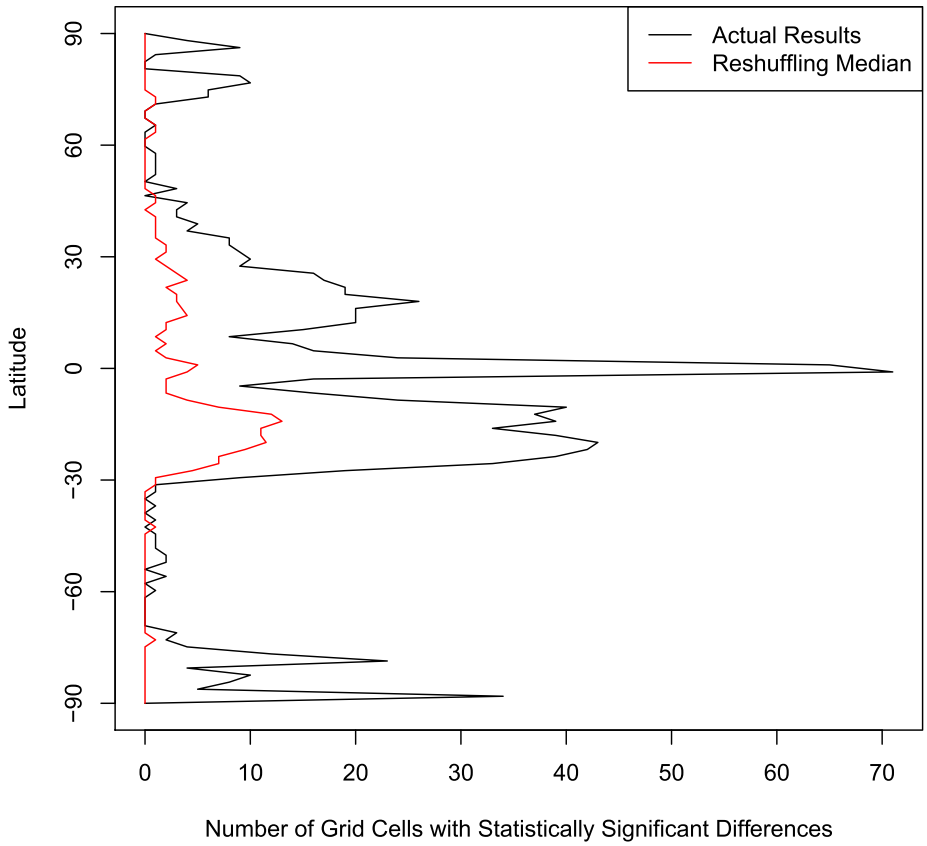

Figure 7. Number of grid cells at each latitude showing statistically significant differences between 1MG and 2MG300 (Table 1) in the ILIAD simulations. ILIAD, InitiaLIzed-ensemble, Analyze, and Develop.

TRMM 3B42's observed extremes generally surpass those of SPCAM's. In particular, our findings of SPCAM's underestimation over eastern CONUS, South America, the eastern equatorial Pacific, and the midlatitude Atlantic Ocean match those of Kooperman et al. (2016), but have a robust, statistical footing here.

4. Conclusions

Earlier studies have found that superparameterization, which is a mechanism to introduce convection-permitting processes into GCMs, can increase the fidelity of the precipitation extremes simulated with these models. However, even as increasing numbers of climate models transition to convection-permitting or -resolving atmospheric dynamics, microphysical processes will still require parameterization. Two previous studies have investigated the sensitivity of microphysics schemes within SP models, though with a regional focus on CONUS. While Elliott et al. (2016) found no discernible signal in summertime MCSs, Charn et al. (2020) found significant differences in extreme precipitation distributions.

Here, we generalize the methodology of Charn et al. (2020) to investigate extreme precipitation globally. Similar to the aforementioned study, the largest differences occur when comparing simulations with different numbers of predicted moments. In a departure from previous findings, disparities persist even during shorter integrations, though primarily only in the tropics (30°S–30°N). Changes in vertical velocities, particularly the column-integrated profiles, were found to be responsible: Two-moment microphysics leads to greater upward motion in the deep tropics and greater subsidence in the subtropics. When looking back to the climatological simulations, changes in vertical velocities become readily apparent at higher latitudes as well. Lastly, we emphasize that differences in both vertical velocity and extreme precipitation in the tropics are amplified when allowing the large-scale circulation time to respond to a new microphysics scheme.

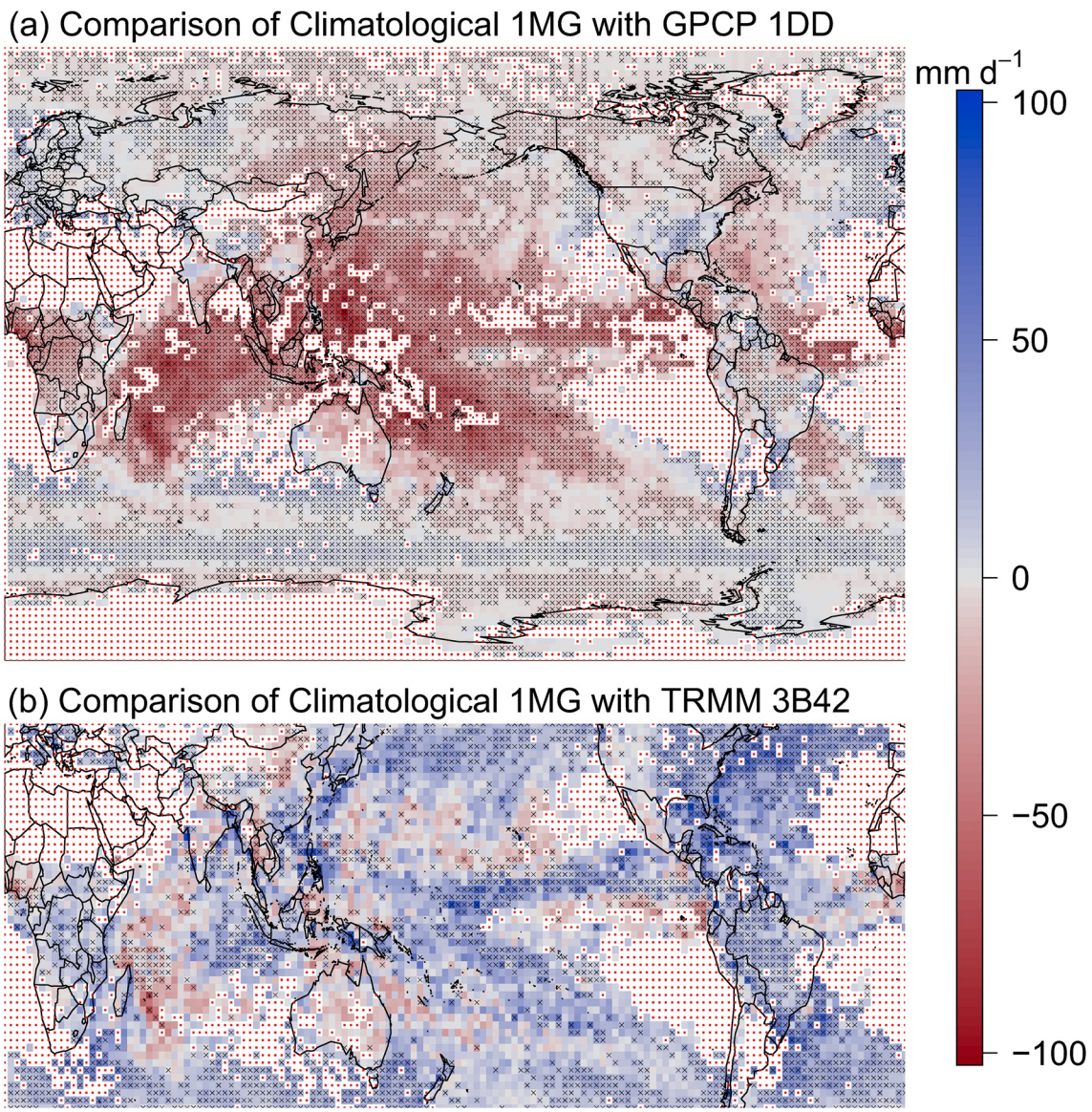

Figure 8. As in Figure 2, but the climatological 1MG (Table 1) 2-year return value is subtracted from that of (a) GPCP 1DD and (b) TRMM 3B42. Comparisons are made using daily data. GPCP, Global Precipitation Climatology Project; TRMM, Tropical Rainfall Measuring Mission.

As elaborated on in Charn et al. (2020), future improvements in microphysics parameterizations, particularly ice processes, would be helpful in terms of simulating clouds and precipitation. In addition, when employing superparameterization, finer resolution and larger domain sizes for the CRMs may be necessary to properly represent organized convection, for example, MCSs (Tao & Chern, 2017). While useful in lowering mean biases in precipitation, given that MCSs supply more than half of rainfall in most tropical regions (Nesbitt et al., 2006) and much of warm-season rainfall in midlatitudes (Schumacher & Johnson, 2006; Zhang et al., 2019), it is reasonable to assume that extreme rain rates would be more faithfully simulated as well.

Appendix A

A1. Controlling the False Discovery Rate

Once α_{FDR}, the level at which it is desired to limit the FDR, is chosen, the procedure for rejecting null hypotheses is as follows. For each comparison between two data sets, and given N finite p-values p_i with $i = 1$,

..., N, sort the p_i into ascending order. Note that N is bounded above by $N \leq 13,824$, the number of GCM grid cells given the resolution used for the GCM spatial grid. Using standard statistical notation, these p-values are now denoted with parenthetical subscripts, such that $p_{(1)} \leq p_{(2)} \leq ... \leq p_{(N)}$. Local null hypotheses are now rejected if their respective p-values are no larger than p_{FDR}:

$$p_{\mathrm{FDR}} = \max_{i=1,..,N} \left[p_{(i)} : p_{(i)} \leq (i / N)\alpha_{\mathrm{FDR}} \right] \tag{A.1}$$

Thus, it can be seen that this method, known as the Benjamini-Hochberg procedure, requires even smaller p-values to reject a local null hypothesis than would be needed when examining individual grid points in isolation.

Data Availability Statement

Tropical Rainfall Measuring Mission data (TMPA Precipitation L3 1 day 0.25° × 0.25° V7) provided by the Goddard Earth Sciences Data and Information Services Center (GES DISC). Global Precipitation Climatology Project data (One-Degree Daily Version 1.3) provided by NCAR at ftp://ftp.cgd.ucar.edu/archive/PRECIP/. The SPCAM model can be accessed at https://doi.org/10.5281/zenodo.3727515. Model data needed to reproduce the figures can be found at https://portal.nersc.gov/project/m1517/cascade/charn2020_spcam_microphys/. The authors would like to thank Travis O'Brien for providing the ILIAD software.

Acknowledgments
This study was supported by the Director, Office of Science, Office of Biological and Environmental Research of the US Department of Energy under Contract no. DE-AC02-05CH11231 as part of their Earth & Environmental Systems Modeling Program and used resources of the National Energy Research Scientific Computing Center (NERSC), also supported by the Office of Science of the US Department of Energy, under Contract no. DE-AC02-05CH11231. Hossein Parishani was supported by the US Department of Energy under Contract no. DE-SC0012548.

References

Benedict, J. J., & Randall, D. A. (2009). Structure of the Madden-Julian oscillation in the superparameterized CAM. *Journal of the Atmospheric Sciences*, *66*(11), 3277–3296. https://doi.org/10.1175/2009jas3030.1

Benjamini, Y., & Hochberg, Y. (1995). Controlling the false discovery rate: A practical and powerful approach to multiple testing. *Journal of the Royal Statistical Society: Series B (Methodological)*, *57*, 289–300. https://doi.org/10.1111/j.2517-6161.1995.tb02031.x

Charn, A. B., Collins, W. D., Parishani, H., Risser, M. D., & O'Brien, T. A. (2020). Microphysical sensitivity of superparameterized precipitation extremes in the contiguous us due to feedbacks on large-scale circulation. *Earth and Space Science*, *7*(7), e2019EA000731. https://doi.org/10.1029/2019ea000731

Dai, A. (2006). Precipitation characteristics in eighteen coupled climate models. *Journal of Climate*, *19*(18), 4605–4630. https://doi.org/10.1175/jcli3884.1

Elliott, E. J., Yu, S., Kooperman, G. J., Morrison, H., Wang, M., & Pritchard, M. S. (2016). Sensitivity of summer ensembles of fledgling superparameterized U.S. mesoscale convective systems to cloud resolving model microphysics and grid configuration. *Journal of Advances in Modeling Earth Systems*, *8*(2), 634–649. https://doi.org/10.1002/2015ms000567

Fan, J., Liu, Y.-C., Xu, K.-M., North, K., Collis, S., Dong, X., et al. (2015). Improving representation of convective transport for scale-aware parameterization: 1. Convection and cloud properties simulated with spectral bin and bulk microphysics. *Journal of Geophysical Research: Atmospheres*, *120*(8), 3485–3509. https://doi.org/10.1002/2014jd022142

Fildier, B., Parishani, H., & Collins, W. D. (2017). Simultaneous characterization of mesoscale and convective-scale tropical rainfall extremes and their dynamical and thermodynamic modes of change. *Journal of Advances in Modeling Earth Systems*, *9*(5), 2103–2119. https://doi.org/10.1002/2017ms001033

Flato, G., Marotzke, J., Abiodun, B., Braconnot, P., Chou, S., Collins, W., et al. (2013). Evaluation of climate models. In T. Stocker, D. Qin, G.-K. Plattner, M. Tignor, S. Allen, J. Boschung (Eds.), *Climate change 2013: The physical science basis. Contribution of Working Group I to the fifth assessment report of the Intergovernmental Panel on Climate Change*. Cambridge University Press.

Held, I. M., & Soden, B. J. (2006). Robust responses of the hydrological cycle to global warming. *Journal of Climate*, *19*(21), 5686–5699. https://doi.org/10.1175/jcli3990.1

Hirota, N., Takayabu, Y. N., Watanabe, M., & Kimoto, M. (2011). Precipitation reproducibility over tropical oceans and its relationship to the double ITCZ problem in CMIP3 and MIROC5 climate models. *Journal of Climate*, *24*(18), 4859–4873. https://doi.org/10.1175/2011jcli4156.1

Huffman, G. J., Adler, R. F., Morrissey, M. M., Bolvin, D. T., Curtis, S., Joyce, R., et al. (2001). Global precipitation at one-degree daily resolution from multisatellite observations. *Journal of Hydrometeorology*, *2*(1), 36–50. https://doi.org/10.1175/1525-7541(2001)002<0036:gpaodd>2.0.co;2

Huffman, G. J., Bolvin, D. T., Nelkin, E. J., Wolff, D. B., Adler, R. F., Gu, G., et al. (2007). The TRMM multisatellite precipitation analysis (TMPA): Quasi-global, multiyear, combined-sensor precipitation estimates at fine scales. *Journal of Hydrometeorology*, *8*(1), 38–55. https://doi.org/10.1175/jhm560.1

Hurrell, J. W., Hack, J. J., Shea, D., Caron, J. M., & Rosinski, J. (2008). A new sea surface temperature and sea ice boundary data set for the community atmosphere model. *Journal of Climate*, *21*(19), 5145–5153. https://doi.org/10.1175/2008jcli2292.1

Hurrell, J. W., Holland, M. M., Gent, P. R., Ghan, S., Kay, J. E., Kushner, P. J., et al. (2013). The community earth system model: A framework for collaborative research. *Bulletin of the American Meteorological Society*, *94*(9), 1339–1360. https://doi.org/10.1175/bams-d-12-00121.1

Jeevanjee, N., & Romps, D. M. (2018). Mean precipitation change from a deepening troposphere. *Proceedings of the National Academy of Sciences of the United States of America*, *115*(45), 11465–11470. https://doi.org/10.1073/pnas.1720683115

Khairoutdinov, M. F., & Randall, D. A. (2001). A cloud resolving model as a cloud parameterization in the NCAR Community Climate System Model: Preliminary results. *Geophysical Research Letters*, *28*(18), 3617–3620. https://doi.org/10.1029/2001gl013552

Khairoutdinov, M. F., & Randall, D. A. (2003). Cloud resolving modeling of the ARM summer 1997 IOP: Model formulation, results, uncertainties, and sensitivities. *Journal of the Atmospheric Sciences*, *60*(4), 607–625. https://doi.org/10.1175/1520-0469(2003)060<0607:crmota>2.0.co;2

Kooperman, G. J., Pritchard, M. S., Burt, M. A., Branson, M. D., & Randall, D. A. (2016). Robust effects of cloud superparameterization on simulated daily rainfall intensity statistics across multiple versions of the community earth system model. *Journal of Advances in Modeling Earth Systems*, *8*(1), 140–165. https://doi.org/10.1002/2015ms000574

Li, F., Rosa, D., Collins, W. D., & Wehner, M. F. (2012). "Super-parameterization": A better way to simulate regional extreme precipitation? *Journal of Advances in Modeling Earth Systems*, *4*(2), M04002. https://doi.org/10.1029/2011ms000106

McCrary, R. R., Randall, D. A., & Stan, C. (2014). Simulations of the west African monsoon with a superparameterized climate model. Part II: African easterly waves. *Journal of Climate*, *27*(22), 8323–8341. https://doi.org/10.1175/jcli-d-13-00677.1

Morrison, H., Curry, J. A., & Khvorostyanov, V. I. (2005). A new double-moment microphysics parameterization for application in cloud and climate models. Part I: Description. *Journal of the Atmospheric Sciences*, *62*(6), 1665–1677. https://doi.org/10.1175/jas3446.1

Nesbitt, S. W., Cifelli, R., & Rutledge, S. A. (2006). Storm morphology and rainfall characteristics of TRMM precipitation features. *Monthly Weather Review*, *134*(10), 2702–2721. https://doi.org/10.1175/mwr3200.1

O'Brien, T. A., Collins, W. D., Kashinath, K., Rübel, O., Byna, S., Gu, J., et al. (2016). Resolution dependence of precipitation statistical fidelity in hindcast simulations. *Journal of Advances in Modeling Earth Systems*, *8*(2), 976–990.

O'gorman, P. A., & Schneider, T. (2009). Scaling of precipitation extremes over a wide range of climates simulated with an idealized GCM. *Journal of Climate*, *22*(21), 5676–5685.

Patricola, C. M., & Wehner, M. F. (2018). Anthropogenic influences on major tropical cyclone events. *Nature*, *563*(7731), 339–346. https://doi.org/10.1038/s41586-018-0673-2

PickandsIII, J. (1971). The two-dimensional Poisson process and extremal processes. *Journal of Applied Probability*, *8*(4), 745–756. https://doi.org/10.1017/s0021900200114640

Risser, M. D., & Wehner, M. F. (2017). Attributable human-induced changes in the likelihood and magnitude of the observed extreme precipitation during hurricane Harvey. *Geophysical Research Letters*, *44*(24), 12457–12464. https://doi.org/10.1002/2017gl075888

Romps, D. M. (2011). Response of tropical precipitation to global warming. *Journal of the Atmospheric Sciences*, *68*(1), 123–138. https://doi.org/10.1175/2010jas3542.1

Saha, S., Moorthi, S., Pan, H.-L., Wu, X., Wang, J., Nadiga, S., et al. (2010). The NCEP climate forecast system reanalysis. *Bulletin of the American Meteorological Society*, *91*(8), 1015–1058. https://doi.org/10.1175/2010bams3001.1

Schumacher, R. S., & Johnson, R. H. (2006). Characteristics of US extreme rain events during 1999–2003. *Weather and Forecasting 21* 69–85. https://doi.org/10.1175/WAF900.1

Singh, M. S., & O'Gorman, P. A. (2012). Upward shift of the atmospheric general circulation under global warming: Theory and simulations. *Journal of Climate*, *25*(23), 8259–8276. https://doi.org/10.1175/jcli-d-11-00699.1

Tao, W. K., & Chern, J. D. (2017). The impact of simulated mesoscale convective systems on global precipitation: A multiscale modeling study. *Journal of Advances in Modeling Earth Systems*, *9*(2), 790–809. https://doi.org/10.1002/2016ms000836

Van Weverberg, K., Vogelmann, A. M., Morrison, H., & Milbrandt, J. A. (2012). Sensitivity of idealized squall-line simulations to the level of complexity used in two-moment bulk microphysics schemes. *Monthly Weather Review*, *140*(6), 1883–1907. https://doi.org/10.1175/mwr-d-11-00120.1

Verlinde, J., & Cotton, W. R. (1993). Fitting microphysical observations of nonsteady convective clouds to a numerical model: An application of the adjoint technique of data assimilation to a kinematic model. *Monthly Weather Review*, *121*(10), 2776–2793. https://doi.org/10.1175/1520-0493(1993)121<2776:fmoonc>2.0.co;2

Wilcox, E. M., & Donner, L. J. (2007). The frequency of extreme rain events in satellite rain-rate estimates and an atmospheric general circulation model. *Journal of Climate*, *20*(1), 53–69. https://doi.org/10.1175/jcli3987.1

Wilks, D. S. (2016). "The stippling shows statistically significant grid points": How research results are routinely overstated and overinterpreted, and what to do about it. *Bulletin of the American Meteorological Society*, *97*(12), 2263–2273. https://doi.org/10.1175/bams-d-15-00267.1

Wilks, S. S. (1938). The large-sample distribution of the likelihood ratio for testing composite hypotheses. *Annals of Mathematical Statistics*, *9*(1), 60–62. https://doi.org/10.1214/aoms/1177732360

Woelfle, M. D., Yu, S., Bretherton, C. S., & Pritchard, M. S. (2018). Sensitivity of coupled tropical pacific model biases to convective parameterization in cesm1. *Journal of Advances in Modeling Earth Systems*, *10*(1), 126–144. https://doi.org/10.1002/2017ms001176

Zhang, G. J., & McFarlane, N. A. (1995). Sensitivity of climate simulations to the parameterization of cumulus convection in the Canadian climate centre general circulation model. *Atmosphere-Ocean*, *33*(3), 407–446. https://doi.org/10.1080/07055900.1995.9649539

Zhang, L., Min, J., Zhuang, X., & Schumacher, R. S. (2019). General features of extreme rainfall events produced by MCSs over East China during 2016-17. *Monthly Weather Review*, *147*(7), 2693–2714. https://doi.org/10.1175/mwr-d-18-0455.1